

The broken link between space and time in elastic turbulence

Giulio Foggi Rota ^a, Rahul K. Singh ^a, Alessandro Chiarini ^{a,c}, Christian Amor ^a, Giovanni Soligo ^a, Dhrubaditya Mitra ^b, Marco Edoardo Rosti ^{a,*}

^a*Complex Fluids and Flows Unit, Okinawa Institute of Science and Technology Graduate University, 1919-1 Tancha, 904-0495, Onna-son, Okinawa, Japan*

^b*Nordita, KTH Royal Institute of Technology and Stockholm University, Hannes Alfvéns väg 12, SE-106 91, Stockholm, Sweden*

^c*Currently at: Dipartimento di Scienze e Tecnologie Aeroespaziali, Politecnico di Milano, via La Masa 34, 20156, Milano, Italy*

Abstract

Elastic turbulence (ET), observed in flows of sufficiently elastic polymer solution at small inertia, is characterized by chaotic motions and power-law scaling of energy spectrum (E) in both wavenumber (k) and frequency (ω): $E(k) \sim k^{-\alpha}$ and $E(\omega) \sim \omega^{-\beta}$. Experiments of ET have obtained a vast range of values for the exponent β . In inertial turbulence, Taylor's frozen-flow hypothesis implies $\alpha = \beta$, i.e., spatial and temporal scales are linearly related to each other. In contrast, from high-resolution simulation in three different setups, a tri-periodic box, a channel, and a planar jet, we show that in ET $\alpha \approx 4$ while β varies significantly. Our analysis shows that in general Taylor's hypothesis does not hold in ET as there is no universal relation, linear or otherwise, between space and time. We thus clear the confusion of the different scaling exponents found in ET, and focus the attention of future research on understanding α . Our analysis also implies that waves-like dynamics with a linear dispersion relation (e.g., Alfvén waves) can not play a role in determining the scaling behavior of ET. The techniques introduced here can be useful for studying smooth chaotic flows in general, e.g., active turbulence.

1. Introduction

Elastic turbulence (ET) [1] is the chaotic state attained by polymeric fluids in flow conditions where elasticity dominates over inertia. Elastic turbulence was first discovered in the early 2000s [2], and it has been investigated experimentally, numerically, and theoretically ever after. Its footprint is a power-law decay of the energy spectrum $E(k) \sim k^{-\alpha}$, similar to what is observed in *inertial turbulence* (IT) [3, 4], although the actual exponent of the power-law is different. Yet, we note that most experimental results in ET are time series of the fluctuating velocity at one point in space, yielding a frequency-dependent energy spectrum with power-law scaling $E(\omega) \sim \omega^{-\beta}$. On one hand, both experimental and numerical results [2, 5, 6, 7, 8, 9, 10, 11, 12, 1, 13, 14, 15, 16, 17, 18, 19] report a vast range of values for

the exponent β , as shown in figure 1. On the other hand, numerical and theoretical investigations [20, 21, 22, 23, 24, 25, 26, 27, 28, 29, 30, 31, 32] identify a narrower range for α , with recent works converging towards a power-law decay in the wavenumbers with exponent $\alpha \approx 4$ common to multiple flow configurations [22, 31, 32, 33] (with few exceptions in two dimensions, explained in Appendix A).

Simulations provide access to the whole flow field, allowing for a direct computation of the spatial as well as the temporal energy spectra, and thereby a measurement of both the exponents α and β . In experiments, it is instead common to work with temporal measurements, recovering the temporal exponent β . The two exponents are typically related applying *Taylor's frozen turbulence hypothesis*, proposed by G. I. Taylor in 1938 [34] to relate the spatial and temporal statistics of grid turbulence in Newtonian flows. He reasoned that, if the intensity of the turbulent velocity fluctuations u is small compared to the mean flow speed U , then the tem-

*Correspondence
Email address: marco.rosti@oist.jp (Marco Edoardo Rosti 

poral response of the flow at a fixed point in space can be seen as the result of an unchanging spatial pattern convecting uniformly past that point at velocity U . In other words, if Taylor's hypothesis holds, there is a linear relationship between space (or the wavenumber k) and time (or the frequency ω) mediated by the mean flow speed U , such that $\omega = U k$, leading to $\alpha = \beta$. Taylor's hypothesis can be extended to flows without a mean velocity too: indeed, an eddy of size $1/k$ is swept by a large scale eddy of size $1/k_0$ over a time $1/(k u_{k_0})$, thus leading again to $\omega \sim k u_{k_0} \sim k$, and $\alpha = \beta$ [4, 35]. Note that, in most cases the scaling range of the spatial as well as temporal energy spectra is barely a decade, thus the scaling exponents cannot be determined with high accuracy. Nevertheless, the large scatter shown in figure 1 raises questions on the applicability of Taylor's hypothesis in ET, and cannot be attributed to a limited scaling range only. This may be attributed to either of the following two reasons: first, the hypothesis holds in ET but α and β , even though not determined with high accuracy, are *not universal* and depend on how the flow is driven; second, the hypothesis cannot be applied to ET and there is no universal relation, linear or otherwise, between space and time. Here we demonstrate, by analyzing direct numerical simulations of different flows, that the latter is true: Taylor's hypothesis does not hold in ET.

2. Model

Let us start by writing down the governing equations for a dilute polymeric fluid [36, 37], i.e., the Navier–Stokes equations coupled to the evolution equation of the averaged polymers' configuration, described by the Oldroyd-B model:

$$\rho_f (\partial_t u_i + u_j \partial_j u_i) = -\partial_i p + \partial_j \left(2\mu_f S_{ij} + \frac{\mu_p}{\tau_p} C_{ij} \right), \quad (1a)$$

$$\partial_t C_{ij} + u_\kappa \partial_k C_{ij} = C_{ik} \partial_k u_j + C_{kj} \partial_i u_\kappa - \frac{1}{\tau_p} (C_{ij} - \delta_{ij}). \quad (1b)$$

Here, \mathbf{u} is the incompressible velocity field, with $\partial_j u_j = 0$, p is the pressure, \mathbf{S} is the rate-of-strain tensor with components $S_{ij} \equiv (\partial_i u_j + \partial_j u_i)$, μ_f and ρ_f are the dynamic viscosity and the density of the solvent fluid with $\nu_f = \mu_f / \rho_f$ being its kinematic viscosity, μ_p and τ_p are the polymer viscosity and

relaxation time, and \mathbf{C} (with components C_{ij}) is the polymer conformation tensor whose trace C_{kk} is the total end-to-end averaged squared length of the polymer. We use Einstein's notation of repeated indices being summed. Three dimensionless numbers govern the behaviour of the equations 1: the Reynolds number $Re = \mathcal{U}\mathcal{L}/\nu_f$, the Deborah number $De = \mathcal{U}\tau_p/\mathcal{L}$, and the solvent-to-total viscosity ratio $\mathcal{B} = \mu_f/(\mu_p + \mu_f)$, where \mathcal{U} and \mathcal{L} are the characteristic velocity and length scales of the problem. We choose \mathcal{B} close to unity, as we simulate dilute polymer solutions. To study ET, we impose the Reynolds number to be small and the Deborah number to be sufficiently large. We consider three different flow configurations, with increasing complexity: a triperiodic box with an external stirring, a pressure-driven channel flow, and a planar jet. All of them were individually investigated in our former works [32, 38, 17].

3. Setup and Methods

3.1. Box

Our box simulations are performed in a cubic domain of edge-length $\mathcal{L} = 2\pi$, uniformly discretised on 512 grid points along each direction. Periodicity is enforced at each boundary, and the flow develops under an Arnold-Beltrami-Childress (ABC) forcing [39] with unitary amplitudes. To confirm the independence of our results from the forcing adopted, we replicated them with the one proposed by Eswaran and Pope [40], observing no significant variation in the spatial and temporal spectra of the turbulent kinetic energy (see [Appendix A](#)). The ET flow is characterised by a Taylor-scale Reynolds number $Re \approx 40$, a Deborah number $De = 9$, and a viscosity ratio $\mathcal{B} = 0.9$ [as in our former study 32]. To compute Re and De we employ the RMS of the velocity fluctuations \mathcal{U} , the edge-length \mathcal{L} , the total viscosity and the relaxation time of the polymer. The IT flow introduced for comparison is characterised by $Re \approx 145$. In both the ET and IT cases, the energy spectra are computed performing an isotropic average across the whole domain and over 40 successive snapshots homogeneously sampled in $490\mathcal{T}$, with $\mathcal{T} = \mathcal{L}/\mathcal{U}$; the spectra of all three velocity components are summed and integrated over a shell in Fourier space. The temporal fluctuations of the velocity used to attain the temporal spectra and the structure functions, instead, are sampled over the same time with an array of

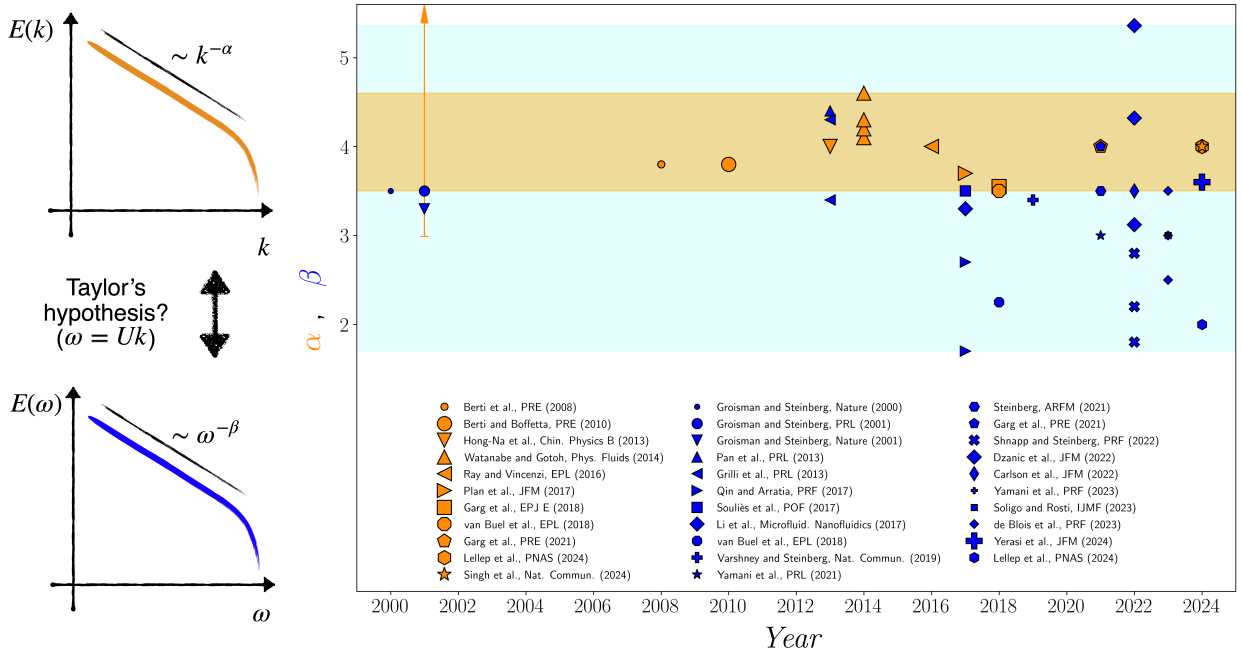


Figure 1: **Power-law spectrum** of the turbulent kinetic energy measured in space and in time for different ET setups over the years. Orange symbols refer to spatial decay exponents α in the wavenumber domain ($k^{-\alpha}$) and blue symbols to temporal decay exponents β in the frequency domain ($\omega^{-\beta}$). The only theoretical prediction is an inequality: $\alpha > 3$, denoted with an arrow. The ranges of variation of the exponents are shown as shaded regions, and highlight the sparsity of the measurements of β compared to those of α , which all lie in a narrow band centred around 4. Notably, no trend for β emerges even reordering the data in terms of the elasticity number (defined as the ratio of Deborah and Reynolds numbers).

128² probes, evenly spaced in a plane crossing the centre of the domain. In this setup, as in all the following, we aimed at ensuring sufficient sampling points for averaging temporal statistics and sufficient proximity between the sampling points to resolve at least the largest scale over which fluctuations remain correlated (with acceptable computational burden). We thus homogeneously distributed the probes every 4 grid points in the selected plane.

3.2. Channel

Our channel simulations are performed in a rectangular domain of size $4\pi\mathcal{L} \times 2\mathcal{L} \times 2\pi\mathcal{L}$ along the streamwise, wall-normal and spanwise directions, uniformly discretised on $512 \times 1024 \times 256$ grid points in the ET case, and in a domain of size $5\mathcal{L} \times 2\mathcal{L} \times 2\mathcal{L}$ uniformly discretised on $1000 \times 400 \times 400$ grid points in the IT case. \mathcal{L} denotes the half-height of the channel. The IT channel simulations are consistent with the minimal flow unit [41] needed to develop and sustain inertial turbulence, resolving all flow structures on a staggered cubic grid with the first node at $z^+ = 0.9$. Instead, in ET, flow

structures are different with large coherent motions spanning the centre of the channel [42] and small-scale perturbations at the walls [43]. We thus employ a larger domain and a finer grid in the wall-normal direction compared to ET to appropriately resolve such features [38]. No-slip and no-penetration boundary conditions are imposed at the top and bottom walls, while periodicity is enforced along the streamwise and spanwise directions. The flow develops under a uniform streamwise pressure gradient, adjusted in time to ensure a constant flow rate. The ET flow is characterised by a bulk Reynolds number $Re = 5$, a Deborah number $De = 50$, and a viscosity ratio $\mathcal{B} = 0.9$ [as in our former study 38]. To compute Re and De we employ the bulk velocity \mathcal{U} , the half-channel height \mathcal{L} , the total viscosity and the relaxation time of the polymer. The IT flow introduced for comparison is characterised by $Re = 5000$. In both the ET and IT cases, the energy spectra are computed at the centre-plane along the streamwise direction, averaged in the spanwise direction and over 220 successive snapshots homogeneously sampled in $100\mathcal{T}$,

summing the spectra of all three velocity components. The temporal fluctuations of the velocity used to attain the temporal spectra and the structure functions are also sampled at the centre-plane over the same time, with an array of 64×32 probes in the ET case and 250×100 probes in the IT case, evenly spaced along the streamwise and spanwise directions, respectively.

3.3. Jet

Our jet simulations are performed in a rectangular domain of size $160\mathcal{L} \times 240\mathcal{L} \times 53.3\mathcal{L}$ along the streamwise, jet-normal and spanwise directions, uniformly discretised on $1536 \times 2304 \times 512$ grid points in the ET case, and in a domain of size $160\mathcal{L} \times 160\mathcal{L} \times 40\mathcal{L}$, uniformly discretised on $3280 \times 3280 \times 820$ grid points in the IT case. The flow is injected from a slit with half-width \mathcal{L} on the left side of the domain at a constant velocity distributed in a plug; the polymers are at rest when injected in the domain. No-slip and no-penetration boundary conditions are enforced at the left wall, exception made for the inlet slit. Free-slip boundary conditions are imposed at the top and bottom boundaries, and a non-reflective outflow is implemented at the right boundary [44]. Periodicity is assumed along the span-wise direction. The ET flow is characterised by an inlet Reynolds number $Re = 20$, a Deborah number $De = 100$, and a viscosity ratio $\mathcal{B} = 0.98$ [as in our former study 17]. To compute Re and De we employ the velocity at the inlet \mathcal{U} , the half-height of the slit through which the fluid is injected \mathcal{L} , the total viscosity and the relaxation time of the polymer. The IT flow introduced for comparison is characterised by $Re = 4500$. In both the ET and IT cases, the energy spectra are computed at the centre-plane along the spanwise direction at a streamwise distance from the inlet of $56\mathcal{L}$ such to ensure fully developed turbulence, averaged over 140 successive snapshots homogeneously sampled in $340\mathcal{T}$, summing the spectra of all three velocity components. The temporal fluctuations of the velocity used to attain the temporal spectra and the structure functions are also sampled at the same location and over the same time, with a line of 128 probes in the ET case and 205 probes in the IT case, evenly spaced along the spanwise direction.

3.4. Numerical Method

The direct numerical simulation of a viscoelastic fluid flow in ET poses significant challenges.

The high-accuracy numerical schemes required for a correct integration of the governing equations and the computational power needed to ensure an adequate resolution make this kind of simulations a remarkable endeavor [45]. In this study, the problem is accurately and efficiently tackled by means of our well validated solver **Fujin** [46, 47, 17]. We adopt a staggered uniform Cartesian grid and discretize equations 1 in space according to a second-order central finite-difference scheme; a second-order Adams–Bashforth scheme is chosen for time integration, coupled with a fractional step method [48]. The transport equation for the polymer conformation tensor **C** requires additional care: we tackle it in a matrix-logarithm formulation [49, 50] to overcome the notorious high Deborah numerical instability and resort to a high-order weighted essentially non-oscillatory (WENO) scheme [51] to treat the upper-convected derivative constituting the left-hand side of equation 1b. In this way we are able to avoid the introduction of a stabilising stress-diffusion term in equation 1b, which therefore does not require us to specify any boundary condition for the polymer [52].

4. Results

The spatial spectra of the turbulent kinetic energy for the instances of a periodic box, a channel, and a jet exhibit a power-law decay of $E(k) \sim k^{-\alpha}$ with $\alpha = 4$, in agreement with previous studies, reported in figure 2. However, the scaling range for the channel and the jet is narrower (less than a decade) compared to that of the box (almost two decades). This result remains unchanged even if (i) we change the model of polymers from Oldroyd-B to FENE-P [32, 38] or PPT [31], (ii) Re is varied within the range 1500 to 0.5 in the channel [38], and (iii) even holds in two dimensions [22]. Yet, the temporal spectra exhibits different $E(\omega) \sim \omega^{-\beta}$ scaling behaviors, with $\beta = 4$ in the box, $\beta = 2$ in the channel, and $\beta = 3$ in the jet. Importantly, for a fixed setup, the scaling of the temporal spectra is robust, e.g. ω^{-3} is observed in jets for a large range of Re [12, 17], from 800 to 20. Note that previous investigations [14] have shown that the slope β varies with the Schmidt number Sc , quantifying polymeric diffusion. Here, however, $Sc \rightarrow +\infty$ as we do not include any explicit diffusion in equation 1b apart from that implicit in the numerics, so our results do not depend from Sc . We thus conclude that, in general, Taylor’s hypothesis does

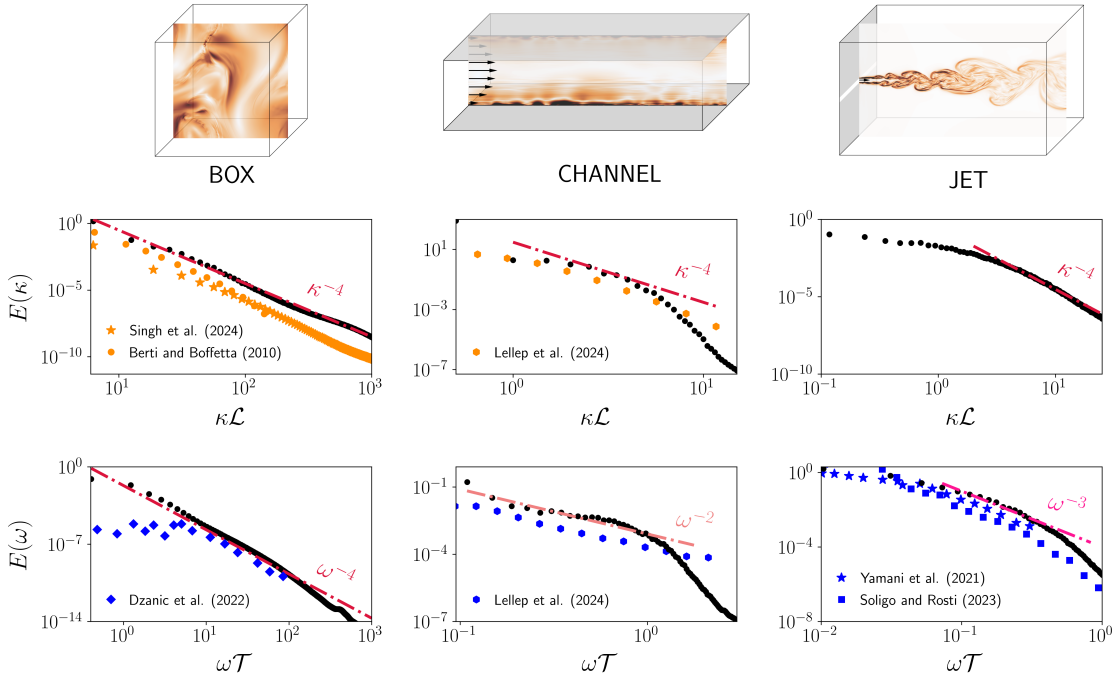


Figure 2: **Turbulent kinetic energy spectra** of elastic turbulence, for box (left), channel (middle) and jet (right), from left to right. Top row: visualizations of the vorticity magnitude, with darker colors denoting higher values. Middle row: spatial energy spectra, normalized with the mean-square of the velocity fluctuations. Bottom row: temporal energy spectra, normalized with the mean square of the velocity fluctuations. *Our data is marked with black dots, while data from literature is highlighted with the same symbols of figure 1 and colors consistent with their spatial/temporal nature. A slight shift downward is applied only to literature data for ease of visualization.* Power-law scalings are reported with dashed-dotted lines.

not hold in ET. In the following, we focus on the channel and the box as prototypical flows with and without a mean velocity.

4.1. A phenomenological approach to the breakdown of Taylor’s hypothesis

Let us now revisit Taylor’s hypothesis in inertial turbulence – high Reynolds number and no polymers – by using phenomenological arguments “à la Kolmogorov”. By Kolmogorov’s phenomenology, the characteristic velocity $u(r)$ at scale $r \ll \mathcal{L}$ is given by $u/\mathcal{U} \sim (r/\mathcal{L})^h$ with $h = 1/3$. Here, \mathcal{U} is the characteristic velocity at the large scale \mathcal{L} . We start by considering equation 1a without the term containing the polymeric stress. The remaining terms yield three distinct characteristic timescales: advection by velocities at large (\mathcal{L}) and small (r) scales give the estimates r/\mathcal{U} , and r/u whereas viscous dissipation gives r^2/ν_f . These three timescales can be rewritten as $(r/\mathcal{L})\mathcal{T}$, $(r/\mathcal{L})^{1-h}\mathcal{T}$, and $(r/\mathcal{L})^2\text{Re}\mathcal{T}$, recalling $\mathcal{T} = \mathcal{L}/\mathcal{U}$. We take the limit $\text{Re} \rightarrow \infty$ and $(r/\mathcal{L}) \rightarrow 0$, thus the fastest

timescale is $(r/\mathcal{L})\mathcal{T}$, i.e., $\tau(r) \sim (r/\mathcal{L})\mathcal{T}$. This linear relationship, $\tau(r) \sim r^z$ with $z = 1$, between time and space is essentially Taylor’s hypothesis (it implies $\omega \sim k$), and the exponent z is called “dynamic exponent”. We mention in passing that this relationship is true only for Eulerian velocities; in Lagrangian [53] or quasi-Lagrangian [54, 55] frames the advection by the large scale velocity can be removed, and within the Kolmogorov model of simple scaling $\tau(r) \sim r^{1-h}$ emerges.

Extending these arguments to ET, we now find four timescales: $(r/\mathcal{L})\mathcal{T}$, $(r/\mathcal{L})^{1-h}\mathcal{T}$, $(r/\mathcal{L})^2\text{Re}\mathcal{T}$, and $(r/\mathcal{L})^2\text{DeRe}\mathcal{T}$. In ET, the velocity field is smooth and $u(r) \sim r^h$ with $h = 1$. For a fixed (small) value of Re and $\text{De} \gg 1$, in the limit $(r/\mathcal{L}) \rightarrow 0$, the fastest timescale is thus $\tau(r) \sim r^2$, which emerges from the viscous term. In practice, however, the presence of a constant (r^0) , which is likely case-dependent, causes no dynamic exponent to emerge: in ET the linear relation between time and space is broken and Taylor’s hypothesis does not hold.

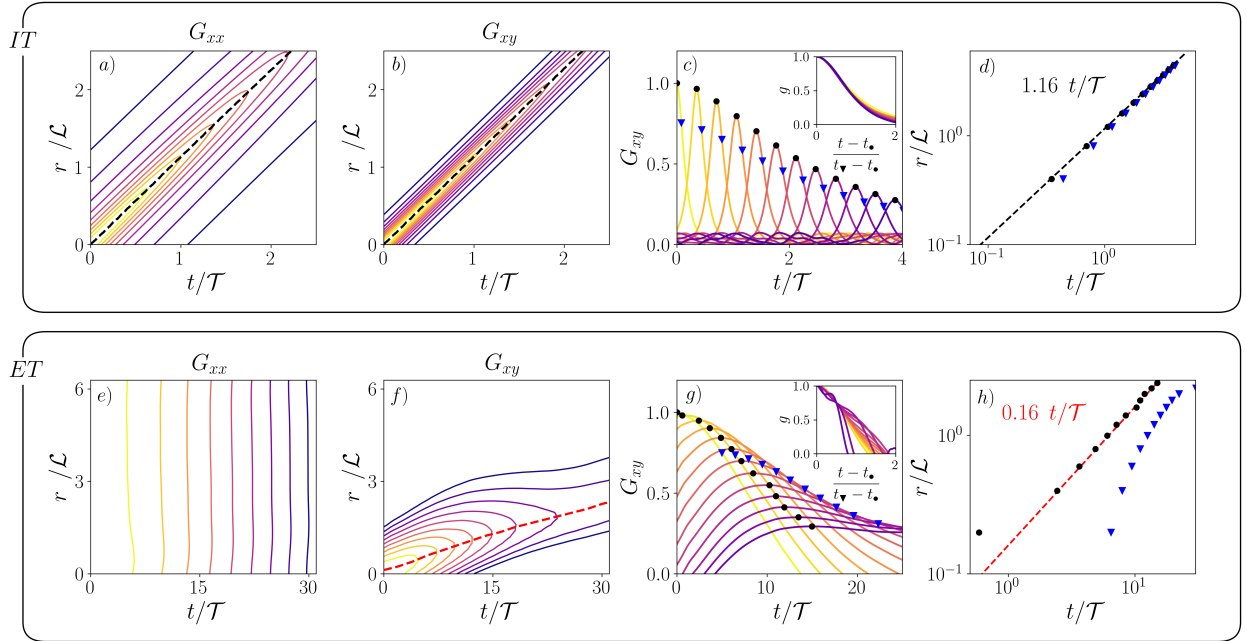


Figure 3: **Space-time relationship in the IT (top row) and ET (bottom row) channel flows.** Contour plots (a,e) of the streamwise autocorrelation of the streamwise velocity component, $G_{xx}(r, t)$, see equation 2b, and (b,f) streamwise autocorrelations of the spanwise velocity component, $G_{xy}(r, t)$, as a function of r/\mathcal{L} and t/\mathcal{T} . The autocorrelations are computed at the center-plane. The contour lines are evenly spaced between 0.1 (blue) and 0.9 (yellow) times the maximum. We also plot (c,g) G_{xy} as a function of t for several different values of r . Black dots demarcate the time of the maximum of G_{xy} , t_\bullet . Blue triangles mark the time, t_∇ , at which G_{xy} falls below a threshold value of 0.75. The insets show the attempted collapse following the ansatz in equation 4, assuming a linear relationship between space and time. We indeed obtain data collapse in IT, but not in ET. Finally, we plot (d,h) the two time-scales extracted from G_{xy} for different length scales. For IT they exhibit the same linear behavior, but for ET different time scales follow different behaviors.

4.2. Space-time relationship in the channel

To develop a clear understanding of the mechanism that leads to the breakdown of Taylor's hypothesis in ET, we revisit the channel flow case comparing and contrasting ET with IT at a Reynolds number $Re = 2800$. We choose a coordinate system such that x is along the streamwise direction, y is along the spanwise direction, and z is along the wall-normal direction. The domain is periodic in x and y , bounded by walls in z . A common way of testing the validity of Taylor's hypothesis in channel flows is by probing the space-time correlation functions of the velocity fluctuations \mathbf{u}

$$\Gamma_{xx}(r, t) = \langle u_x(\mathbf{x} + \hat{\mathbf{x}}r, t) u_x(\mathbf{x}, 0) \rangle,$$

$$\Gamma_{xy}(r, t) = \langle u_y(\mathbf{x} + \hat{\mathbf{x}}r, t) u_y(\mathbf{x}, 0) \rangle; \quad (2a)$$

$$G_{xx}(r, t) = \frac{\Gamma_{xx}(r, t)}{\Gamma_{xx}(0, 0)},$$

$$G_{xy}(r, t) = \frac{\Gamma_{xy}(r, t)}{\Gamma_{xy}(0, 0)}; \quad (2b)$$

where the first subscript indicates the direction along which the correlation is evaluated, and the second the component of velocity considered. Here $\hat{\mathbf{x}}$ is the unit vector along the streamwise direction, and averages $\langle \cdot \rangle$ are done in time and along the homogeneous directions, leaving only the dependence on the space and time separations, r and t . The correlations at the center-plane of the channel relate to the space and time energy spectra plotted in figure 2 as

$$E(k) = \frac{1}{2} \int \sum_i \Gamma_{xi}(r, 0) \exp(ikr) dr, \quad (3)$$

$$E(\omega) = \frac{1}{2} \int \sum_i \Gamma_{xi}(0, t) \exp(i\omega t) dt,$$

respectively.

In figure 3a we show the contour plots of $G_{xx}(r, t)$ as a function of r and t . If Taylor's hypothesis holds, then the slope of the line connecting the spatial maxima of the contours is proportional to the average advective velocity with which fluctuations

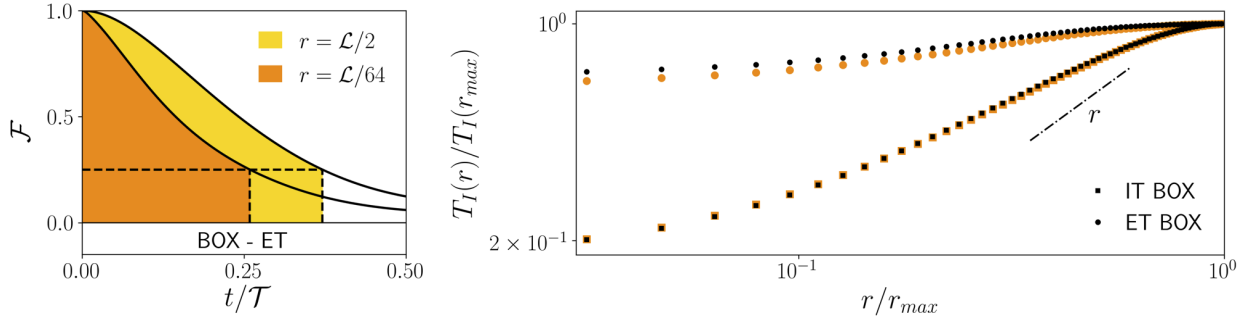


Figure 4: **Dynamic scaling in the box.** (left) A representative plot of $\mathcal{F}(r, t)/\mathcal{F}(r, 0)$ for two values of r for ET in the box. The dashed horizontal line is at the value of ordinate equal to 0.25. The shaded area is the integral scale T_I defined in equation 7 for the case where the threshold is 0.25. (right) The characteristic timescale $T_I(r)$ as a function of r for IT (squares) and ET (circles); blue symbols are for a threshold of 0.25 and black symbols are for the zero-crossing. Note that, the black squares of IT overlap the blue ones. A dashed line with unitary slope is shown to guide the eye.

are transported downstream [56]. At the centerline of the IT channel flow, such velocity is, approximately, $1.16 \mathcal{U}$ [57], where \mathcal{U} for a channel is the mean velocity of the flow. The picture is dramatically different in ET, see figure 3e. Here, the contours are parallel to the ordinate, so no dynamic scaling is observed. Now, let us compare IT and ET for the other correlation function, $G_{xy}(r, t)$. In IT, the contours of figure 3b make it clear that a dynamic exponent $z = 1$ holds. Yet, the situation in ET is again quite different. The peaks of the contours in figure 3f seem to follow an approximately linear space-time relation, but the remaining regions of the contours do not; suggesting that a unique relation between space and time may not exist. To investigate this further, we plot G_{xy} as a function of t for several different values of r in IT and ET in figure 3c,g. In IT, the plots suggest the following data collapse:

$$G_{xy}(r, t) = g \left[\frac{t - t_{\bullet}(r)}{t_{\nabla}(r) - t_{\bullet}(r)} \right] \quad \text{with} \quad (4)$$

$$t_{\bullet}(r) \propto r \quad \text{and} \quad t_{\nabla}(r) \propto r,$$

where $t_{\bullet}(r)$ is the time at which G_{xy} peaks and $t_{\nabla}(r)$ is any other timescale one may choose. In the following, we set $t_{\nabla}(r)$ to be the time at which G_{xy} falls below the threshold value of 0.75. We check in the inset of figure 3c that this collapse indeed holds. In figure 3d we plot both $t_{\bullet}(r)$ and $t_{\nabla}(r)$ on the abscissa, and the corresponding r values on the ordinate. In both cases we obtain a clean linear behaviour. This conclusively proves that in the IT channel flow the dynamic exponent is $z = 1$. We now try the same approach for ET, plotting the

values of $t_{\bullet}(r)$ from figure 3g in figure 3h. They do show a linear trend, but we do not find a collapse for the complete correlation function – see the inset of figure 3g. Next, similar to IT, we also extract $t_{\nabla}(r)$ from G_{xy} in figure 3g and plot its values in figure 3h, with r on the ordinate. We do not find any significant scaling, again demonstrating that there is no dynamic scaling in ET – the link between space and time is broken.

4.3. Space-time relationship in the box

To develop a clearer understanding of the relationship between space and time in ET, we now consider the simple case of a triperiodic box, where the problem is homogeneous and isotropic. Following earlier attempts [58, 59, 60, 61] to understand the space-time nature of IT, we define,

$$\Gamma(r, t) = \langle u_i(\mathbf{x} + \mathbf{r}, 0) u_i(\mathbf{x}, t) \rangle, \quad (5a)$$

$$\delta_{\mathbf{r}} u_i(t) = u_i(\mathbf{x} + \mathbf{r}, t) - u_i(\mathbf{x}, t), \quad (5b)$$

$$\mathcal{F}(r, t) = \langle \delta_{\mathbf{r}} u_i(0) \delta_{\mathbf{r}} u_i(t) \rangle = 2\Gamma(0, t) - 2\Gamma(r, t). \quad (5c)$$

The functions $\Gamma(r, t)$ and $\mathcal{F}(r, t)$ are the space and time dependent second order correlation function and structure function, respectively. They do not depend on \mathbf{x} because of homogeneity, and they only depend on the magnitude of \mathbf{r} , and not on its direction, because of isotropy. The two energy spectra shown before are related to the correlation function by

$$E(k) = \frac{1}{2} \int \Gamma(r, 0) \exp(ikr) dr, \quad (6)$$

$$E(\omega) = \frac{1}{2} \int \Gamma(0, t) \exp(i\omega t) dt.$$

From the time-dependent correlation function, we can define a scale-dependent integral time scale

$$T_I(r) \equiv \frac{1}{\mathcal{F}(r, 0)} \int_0^{T_0} \mathcal{F}(r, t) dt, \quad (7)$$

where T_0 is the time it takes to cross a threshold. We use two values for this threshold, 0.25 and 0. Taylor's hypothesis would imply $T_I(r) \sim r^z$ with $z = 1$. In figure 4 we plot $T_I(r)$ as a function of r in a log-log scale for both IT and ET. In the case of IT, we obtain a small range over which $z = 1$. Similar results have been reported before [62, 61]. For ET, instead, we observe that it is difficult to find any significant scaling range, with the function being almost a constant ($z = 0$), especially at large r . Again, Taylor's hypothesis does not hold; the link between space and time is broken in ET, notwithstanding that both spatial and temporal spectra have $\alpha = \beta = 4$ in the box.

It is possible to develop an approximate understanding of this result in the extreme case of $Re \rightarrow 0$. In this limit, equation 1a reduces to the linear, forced, Stokes equation, which can be solved by Fourier transform. Substituting the solution back in equation 1b, we obtain a nonlinear evolution equation for the tensor C_{ij} . A straightforward scaling analysis of this equation, with the assumption that the scaling exponent for the velocity is $h = 1$ in ET, yields two possible values: $z = 0$ and $z = 2$, see appendix Appendix B. At large r , $z = 0$ dominates over $z = 2$, which is indeed what we observe.

5. Discussions

Several comments are now in order. First, note that the key feature that makes ET different from IT is that the advective nonlinearity is subdominant in ET. We verified that it is reasonable to completely remove the nonlinear advective term from the momentum equation as an approximation, by re-running our ET simulations in the box and the channel with the nonlinear advection turned off (see appendix Appendix C); the energy spectra of the velocity remained practically unchanged. It is thus reasonable to ignore the nonlinear advection in the momentum equation to develop a theoretical description of ET.

Second, multiple investigations in IT have discussed the limitations of Taylor's hypothesis and possible improvements [63, 64, 65, 66, 67, 68, 69, 70,

71, 72, 73, 74, 75, 76, 77]. It has for example been noticed that, in grid turbulence, Taylor's hypothesis does not accurately represent the dilatational part of the flow [67], while it also breaks down in flows with high shear [63]. Issues similar to those encountered when applying Taylor's hypothesis to IT in the presence of coherent structures have been reported also in ET [78], and caution is recommended when investigating higher-order moments based on temporal sampling only [30]. However, here we show that the use of Taylor's hypothesis in ET is fundamentally flawed, unlike in IT.

Third, note that in IT, in a *Lagrangian or quasi-Lagrangian* frame, the dynamical scaling is broken – there is no unique dynamic exponent and dynamical multiscaling holds [58, 59, 60, 79] due to the fundamental multifractal nature of IT. This is not relevant to the breakdown of Taylor's hypothesis, as we have discussed here.

Fourth, the existence of a dynamic exponent $z = 1$ may also mean existence of Alfvén-like waves in ET, as suggested in Ref. [80]. To investigate the possibility of elastic waves (with the same dispersion relation as Alfvén waves), Varshney and Steinberg [11] measured the correlation function $G_{xy}(r, t)$ (as defined in equation 2b) in their experiments, and showed that the peaks of this function follow a linear scaling. The same behavior is observed in figure 3h – consistent with the experimental results. Yet, this scaling only applies to the peaks, not to the whole correlation function (see the absence of collapse in the inset of figure 3g) or to other correlation functions, e.g., G_{xx} . Furthermore, Alfvén waves require the nonlinear advection term to exist, but we have shown that simulations without this term provide the same scaling exponent $\alpha = 4$. Thus, these two points together show that elastic waves with linear dispersion relation do not play a role in determining the scaling behavior of ET.

Finally, in this paper, we clear the confusion of many different scaling exponents for the energy spectrum of ET. As shown in fig. 1, over the years experiments and simulations have obtained a large range of scaling exponents. With time, the spatial exponent α is converging to 4, but the temporal exponent β varies over a large range. We now establish that, due to breakdown of Taylor's hypothesis, β is not universal. The focus of theory in ET should be to understand the $\alpha \approx 4$ scaling of the spatial energy spectrum.

Acknowledgments

The research was supported by the Okinawa Institute of Science and Technology Graduate University (OIST) with subsidy funding to M.E.R. from the Cabinet Office, Government of Japan. M.E.R. also acknowledges funding from the Japan Society for the Promotion of Science (JSPS), grants 24K00810 and 24K17210. The authors acknowledge the computer time provided by the Scientific Computing Section and Data Analysis section of the Core Facilities at OIST, and the computational resources provided by RIKEN, under the HPCI System Research Project Grants hp250021, hp250035, hp230018, hp220099, hp210269, and hp210229. DM acknowledges the support of the Swedish Research Council Grant No. 638-2013-9243. DM gratefully acknowledges hospitality by OIST. M.E.R. and G.F.R. acknowledge the useful discussion with Prof. Guido Boffetta and Stefano Musacchio.

Author contributions

G.F.R. analysed the data. G.F.R., R.K.S., D.M., and M.E.R. developed the theory, with inputs from A.C.. G.F.R., C.A., G.S., and M.E.R. developed the simulation code. G.S. and M.E.R. performed the numerical simulations. G.F.R., D.M., and M.E.R. outlined the manuscript content and finalised the manuscript, with the first draft written by G.F.R., and inputs from all authors. D.M. and M.E.R. conceived the original idea and supervised the research.

Appendix A. Independence of the results from the forcing

To confirm the independence of our results from the forcing adopted, we replicated them with the one proposed by Eswaran and Pope [40], observing no significant variation in the spatial and temporal spectra of the turbulent kinetic energy (figure 5). No significant variation is observed in the spectral decay, regardless of the forcing adopted (ABC in black, Pope in orange), thus confirming the generality of our observations. Both the spatial (left) and temporal (right) spectra approach the power-law decay with exponent -4 discussed in the main text. Note that this might not hold in two dimensions, where α was shown to vary between -3 and -4 depending on the forcing chosen [27, 81, 19].

Appendix B. Theory for the dynamics of ET in a periodic box

We consider the Oldroyd-B equation [37] in a homogeneous and isotropic setup, forced by an external stirring:

$$\rho_f (\partial_t u_\alpha + u_\beta \partial_\beta u_\alpha) = -\partial_\alpha p + \partial_\beta \left(2\mu_f S_{\alpha\beta} + \frac{\mu_p}{\tau_p} C_{\alpha\beta} \right) + \rho_f f_\alpha \quad (B.1a)$$

$$-t C_{\alpha\beta} + u_\gamma \partial_\gamma C_{\alpha\beta} = C_{\alpha\gamma} \partial_\gamma u_\beta + C_{\gamma\beta} \partial_\alpha u_\gamma - \frac{1}{\tau_p} (C_{\alpha\beta} - \delta_{\alpha\beta}). \quad (B.1b)$$

Here, \mathbf{u} is the incompressible solvent velocity field, i.e. $\partial_\beta u_\beta = 0$, p is the pressure, \mathcal{S} is the rate-of-strain tensor with components $S_{\alpha\beta} \equiv (\partial_\alpha u_\beta + \partial_\beta u_\alpha)$, μ_f is the dynamic viscosity of the solvent and $\nu_f = \mu_f / \rho_f$ is its kinematic viscosity, μ_p is the polymer viscosity, ρ_f is the density of the solvent fluid, τ_p is the polymer relaxation time, and \mathbf{C} is the polymer conformation tensor whose trace $C_{\gamma\gamma}$ is the total end-to-end squared length of the polymer. We use Einstein's notation of repeated indices being summed and the symbol $\langle \cdot \rangle$ denotes averaging over turbulence.

Appendix B.1. Non-dimensionalization

We use the following scheme for non-dimensionalization:

$$\mathbf{x}^* = \frac{\mathbf{x}}{\mathcal{L}}, \quad t^* = \frac{t}{\tau_p}, \quad \mathbf{u}^* = \frac{\mathbf{u}}{\mathcal{U}}, \quad p^* = \frac{p}{\rho_f \mathcal{U}^2}. \quad (B.2)$$

We denote by the superscript $*$ the non-dimensional form of any quantity. The tensor $C_{\alpha\beta}$ is already dimensionless. For the homogeneous and isotropic case we use $\mathcal{U} = u_{\text{rms}}$ and non-dimensionalize the external force by its amplitude F . Consequently the non-dimensional form of the PDEs (equation B.1) becomes:

$$\frac{1}{\text{De}} \partial_t^* u_\alpha^* + u_\beta^* \partial_\beta^* u_\alpha^* = -\partial_\alpha^* p^* + \frac{\mathcal{B}}{\text{Re}} \partial_\beta^* 2S_{\alpha\beta}^* + \frac{1-\mathcal{B}}{\text{ReDe}} \partial_\beta^* C_{\alpha\beta}^* + \frac{1}{\text{Fr}} f_\alpha^*, \quad (B.3a)$$

$$\frac{1}{\text{De}} [\partial_\gamma^* C_{\alpha\beta}^* + C_{\alpha\beta}^* - \delta_{\alpha\beta}] = -u_\gamma^* \partial_\gamma^* C_{\alpha\beta}^* + C_{\alpha\gamma}^* \partial_\gamma^* u_\beta^* + C_{\gamma\beta}^* \partial_\alpha^* u_\gamma^*. \quad (B.3b)$$

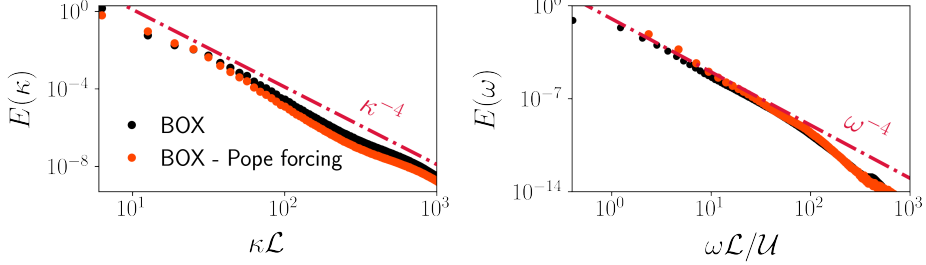


Figure 5: **Turbulent kinetic energy spectra with Pope's forcing** in our box setup, normalised with the mean-square of the velocity fluctuations.

Four dimensionless numbers govern the qualitative behavior of these equations: the Reynolds number $Re = \mathcal{U}\mathcal{L}/\nu_f$; the Deborah number $De = \mathcal{U}\tau_p/\mathcal{L}$; the solvent-to-total-viscosity ratio $\mathcal{B} = \mu_f/(\mu_p + \mu_f)$; and the Froude number $Fr = \mathcal{U}^2/(\mathcal{L}F)$. As we simulate a dilute polymer solution, we choose a fixed value for \mathcal{B} in all our simulations.

Appendix B.2. Small Re approximation

To study ET we choose the Reynolds number to be small and the Deborah number to be sufficiently large. We hold De to be constant, take the limit $Re \rightarrow 0$ and substitute $p^\dagger = Re p^*$ [82]. In taking this limit, we assume that Re/Fr remains unity. We then obtain

$$\mathcal{B}(\nabla^2)^* u_\alpha^* = \partial_\alpha^* p^\dagger - \frac{1-\mathcal{B}}{De} \partial_\beta^* C_{\alpha\beta}^* - f_\alpha^*, \quad (B.4a)$$

$$\frac{1}{De} [\partial_t^* C_{\alpha\beta}^* + C_{\alpha\beta}^* - \delta_{\alpha\beta}] = -u_\gamma^* \partial_\gamma^* C_{\alpha\beta}^* + C_{\alpha\gamma}^* \partial_\gamma^* u_\beta^* + C_{\gamma\beta}^* \partial_\alpha^* u_\gamma^*. \quad (B.4b)$$

Here, we have assumed incompressibility to simplify the viscous stress and the external force. From here on, we drop the superscripts – it is assumed that the variables are dimensionless. The equations are thus rewritten as:

$$\partial_\alpha u_\alpha = 0, \quad (B.5a)$$

$$\mathcal{B}\nabla^2 u_\alpha = \partial_\alpha p - \frac{1-\mathcal{B}}{De} \partial_\beta C_{\alpha\beta} + f_\alpha, \quad (B.5b)$$

$$\partial_t C_{\alpha\beta} = \delta_{\alpha\beta} - C_{\alpha\beta} + De [C_{\alpha\gamma} \partial_\gamma u_\beta + C_{\gamma\beta} \partial_\alpha u_\gamma - u_\gamma \partial_\gamma C_{\alpha\beta}]. \quad (B.5c)$$

In the absence of polymers, $\mu_p = 0$, $\mathcal{B} = 1$. Consequently, equation B.5 reduces to the incompressible, forced Stokes equation.

Appendix B.3. In Fourier space

Next, we Fourier transform in space (but not in time) and impose incompressibility by multiplying equation B.5b by the projection operator

$$\mathcal{P}_{\alpha\beta}(\mathbf{k}) \equiv \delta_{\alpha\beta} - \frac{k_\alpha k_\beta}{k^2}, \quad (B.6)$$

where \mathbf{k} is the Fourier vector. We obtain:

$$\mathcal{B}k^2 u_\beta(\mathbf{k}) = -i \frac{1-\mathcal{B}}{De} \mathcal{P}_{\alpha\beta} k_\gamma C_{\alpha\gamma} + \mathcal{P}_{\alpha\beta} f_\alpha, \quad (B.7)$$

We use the same symbol for variables and their Fourier transforms. The Fourier transform of equation B.5c is

$$\begin{aligned} \partial_t C_{\alpha\beta}(\mathbf{k}) &= \delta_{\alpha\beta} \delta(\mathbf{k}) - C_{\alpha\beta}(\mathbf{k}) \\ &\quad - iDe \int d^d p d^d q \delta(\mathbf{k} - \mathbf{p} - \mathbf{q}) \\ &[p_\gamma u_\beta(\mathbf{p}) C_{\alpha\gamma}(\mathbf{q}) + p_\alpha u_\gamma(\mathbf{p}) C_{\gamma\beta}(\mathbf{q}) - q_\gamma u_\gamma(\mathbf{p}) C_{\alpha\beta}(\mathbf{q})]. \end{aligned} \quad (B.8)$$

Substituting equation B.7 to equation B.8 we obtain

$$\begin{aligned} \partial_t C_{\alpha\beta}(\mathbf{k}) &= \delta_{\alpha\beta} \delta(\mathbf{k}) - C_{\alpha\beta}(\mathbf{k}) \\ &\quad - \frac{1-\mathcal{B}}{\mathcal{B}} \int_{\mathbf{p}, \mathbf{q}} \left[\frac{p_\kappa p_\gamma}{p^2} \mathcal{P}_{\delta\beta} C_{\delta\gamma}(\mathbf{p}) C_{\alpha\kappa}(\mathbf{q}) \right. \\ &\quad \left. + \frac{p_\alpha p_\gamma}{p^2} \mathcal{P}_{\delta\kappa} C_{\delta\gamma}(\mathbf{p}) C_{\kappa\beta}(\mathbf{q}) \right. \\ &\quad \left. - \frac{q_\gamma p_\kappa}{p^2} \mathcal{P}_{\delta\gamma} C_{\delta\kappa}(\mathbf{p}) C_{\alpha\beta}(\mathbf{q}) \right] \\ &\quad - i \frac{De}{\mathcal{B}} \int_{\mathbf{p}, \mathbf{q}} \frac{1}{p^2} \left[p_\gamma f_\beta(\mathbf{p}) C_{\alpha\gamma}(\mathbf{q}) + p_\alpha f_\gamma(\mathbf{p}) C_{\gamma\beta}(\mathbf{q}) \right. \\ &\quad \left. - q_\gamma f_\gamma(\mathbf{p}) C_{\alpha\beta}(\mathbf{q}) \right], \end{aligned} \quad (B.9a)$$

where $\int_{\mathbf{p}, \mathbf{q}} \equiv \int d^d p d^d q \delta(\mathbf{k} - \mathbf{p} - \mathbf{q})$, and the argument of \mathcal{P} , \mathbf{p} , is not explicitly written. Here $d = 3$ is the dimension of space. Altogether this is an intriguing term, which demonstrates the following. One, even when the external force is limited to a single Fourier shell, it appears in a convolution in equation B.9a, i.e., its effects are felt at all scales. Two, the force multiplies the tensor $C_{\alpha\beta}$, hence if the force is random and Gaussian it appears as a *multiplicative noise*.

Appendix B.4. Scaling analysis

Let us now perform a straightforward scaling analysis (see e.g., [4, section 9.6.4]) of equation B.9a. We rewrite the equations as

$$\begin{aligned} \partial_t C_{\alpha\beta}(\mathbf{k}) &= \delta_{\alpha\beta} \delta(\mathbf{k}) - C_{\alpha\beta}(\mathbf{k}) \\ &+ \square(C, C) + \Delta(C, F), \end{aligned} \quad (\text{B.10a})$$

$$\begin{aligned} \square(C, C) &= -\frac{1-\mathcal{B}}{\mathcal{B}} \int_{\mathbf{p}, \mathbf{q}} \left[\frac{p_\kappa p_\gamma}{p^2} \mathcal{P}_{\delta\beta} C_{\delta\gamma}(\mathbf{p}) C_{\alpha\kappa}(\mathbf{q}) \right. \\ &+ \frac{p_\alpha p_\gamma}{p^2} \mathcal{P}_{\delta\kappa} C_{\delta\gamma}(\mathbf{p}) C_{\kappa\beta}(\mathbf{q}) \\ &\left. - \frac{q_\gamma p_\kappa}{p^2} \mathcal{P}_{\delta\gamma} C_{\delta\kappa}(\mathbf{p}) C_{\alpha\beta}(\mathbf{q}) \right], \end{aligned} \quad (\text{B.10b})$$

$$\begin{aligned} \Delta(C, F) &= -i \frac{\text{De}}{\mathcal{B}} \int_{\mathbf{p}, \mathbf{q}} \frac{1}{p^2} \left[p_\gamma f_\beta(\mathbf{p}) C_{\alpha\gamma}(\mathbf{q}) \right. \\ &+ p_\alpha f_\gamma(\mathbf{p}) C_{\gamma\beta}(\mathbf{q}) \\ &\left. - q_\gamma f_\gamma(\mathbf{p}) C_{\alpha\beta}(\mathbf{q}) \right], \end{aligned} \quad (\text{B.10c})$$

Now, consider the scaling

$$x \rightarrow bx, \quad t \rightarrow b^z t, \quad \text{and} \quad k \rightarrow k/b, \quad (\text{B.11})$$

so that the fields in real space scale as

$$\mathbf{u}(\mathbf{x}) \rightarrow b^h \mathbf{u}(\mathbf{x}), \quad \text{and} \quad C_{\alpha\beta}(\mathbf{x}) \rightarrow b^m C_{\alpha\beta}(\mathbf{x}). \quad (\text{B.12})$$

The Fourier transforms of the same fields, of course, scale differently:

$$\mathbf{u}(\mathbf{k}) \rightarrow b^\chi \mathbf{u}(\mathbf{k}), \quad \text{and} \quad C_{\alpha\beta}(\mathbf{k}) \rightarrow b^\xi C_{\alpha\beta}(\mathbf{k}), \quad (\text{B.13})$$

where $\chi = h + d$ and $\xi = m + d$, follows from the definition of Fourier transform. We use a force that is constant in time and limited to a few small

Fourier modes. Thus, under rescaling, the force remains constant. Then the different terms in equation B.10c scale as

$$\begin{aligned} \partial_t C_{\alpha\beta} &\rightarrow b^{\xi-z} \partial_t C_{\alpha\beta}, \quad C_{\alpha\beta} \rightarrow b^\xi C_{\alpha\beta}, \\ \square &\rightarrow b^{2\xi-d} \square, \quad \Delta \rightarrow b^{\xi-d+1} \Delta. \end{aligned} \quad (\text{B.14})$$

Here, we have ignored the term $\delta(\mathbf{k})$ as it is zero for all \mathbf{k} except for $\mathbf{k} = 0$. Assuming that equation B.10c is scale invariant, we now obtain the following relations

$$\xi - z = \xi \implies z = 0, \quad (\text{B.15a})$$

$$\xi - z = 2\xi - d \implies z = d - \xi, \quad (\text{B.15b})$$

$$\xi - z = \xi - d + 1 \implies z = d - 1. \quad (\text{B.15c})$$

From eq. B.5b we obtain: $h - 2 = m - 1 = \xi - d - 1$, and substituting this in eq. B.5b and simplifying, we obtain the following three choices:

$$z = 0, \quad z = 1 - h, \quad \text{and} \quad z = d - 1 = 2. \quad (\text{B.16})$$

In ET we know that $h = 1$, hence the first two expressions are consistent with each other, but the last one is not. Even if the force is limited to a few Fourier modes, since the term Δ is a convolution, its effects are present in all modes and cannot be considered small anywhere. Thus we conclude that there is no unique dynamic scaling exponent in ET.

Appendix C. Neglecting the non-linear advection

To assess the role played in ET by the non-linear advection term, $u_\beta \partial_\beta u_\alpha$, we perform two additional simulations in the box and channel setups where this term is explicitly removed from the momentum equation. We do not observe any significant change to the spatial spectra of the turbulent kinetic energy in either of these cases, see figure B.6. The spectra exhibit a clear k^{-4} power-law decay for the box (over almost two decades) and the channel (little more than half a decade).

References

- [1] V. Steinberg. Elastic Turbulence: An Experimental View on Inertialess Random Flow. *Annu. Rev. Fluid Mech.*, 53(1):27–58, 2021.
- [2] A. Groisman and V. Steinberg. Elastic turbulence in a polymer solution flow. *Nature*, 405(6782):53–55, May 2000.

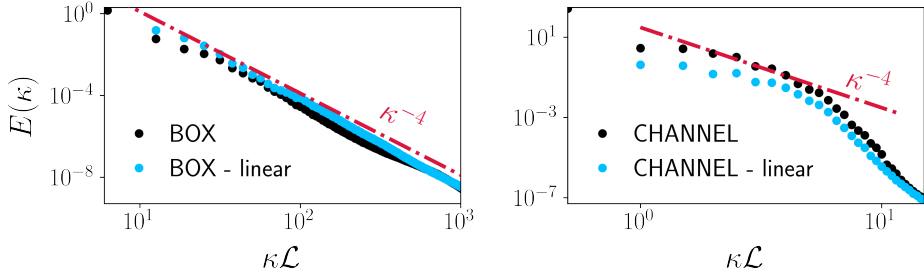


Figure B.6: **Turbulent energy spectra with and without nonlinear advection** in box (left) and channel (right) setups. In black: spectra from solving the Navier-Stokes equation together with the Oldroyd-B model, equation B.1. In blue: spectra with the nonlinear advection term ignored. The two spectra have close overlap, both show k^{-4} scaling. The spectra are normalised with the mean-square of the velocity fluctuations.

- [3] A. N. Kolmogorov. The Local Structure of Turbulence in an Incompressible Viscous Fluid for Very Large Reynolds Numbers. *Dokl. Akad. Nauk. SSSR*, 30:301–305, 1941.
- [4] U. Frisch. *Turbulence: The Legacy of A. N. Kolmogorov*. Cambridge University Press, November 1995.
- [5] A. Groisman and V. Steinberg. Stretching of Polymers in a Random Three-Dimensional Flow. *Phys. Rev. Lett.*, 86(5):934–937, 2001.
- [6] Alexander Groisman and Victor Steinberg. Efficient mixing at low Reynolds numbers using polymer additives. *Nature*, 410(6831):905–908, April 2001.
- [7] L. Pan, A. Morozov, C. Wagner, and P. E. Arratia. Nonlinear Elastic Instability in Channel Flows at Low Reynolds Numbers. *Phys. Rev. Lett.*, 110(17):174502, 2013.
- [8] M. Grilli, A. Vázquez-Quesada, and M. Ellero. Transition to Turbulence and Mixing in a Viscoelastic Fluid Flowing Inside a Channel with a Periodic Array of Cylindrical Obstacles. *Phys. Rev. Lett.*, 110(17):174501, 2013.
- [9] B. Qin and P. E. Arratia. Characterizing elastic turbulence in channel flows at low Reynolds number. *Phys. Rev. Fluids*, 2(8):083302, 2017.
- [10] A. Souliès, J. Aubril, C. Castelain, and T. Burghelea. Characterisation of elastic turbulence in a serpentine micro-channel. *Phys. Fluids*, 29(8):083102, 2017.
- [11] A. Varshney and V. Steinberg. Elastic Alfvén waves in elastic turbulence. *Nat. Commun.*, 10(1):652, February 2019.
- [12] S. Yamani, B. Keshavarz, Y. Raj, T. A. Zaki, G. H. McKinley, and I. Bischofberger. Spectral Universality of Elastoinertial Turbulence. *Phys. Rev. Lett.*, 127(7):074501, August 2021.
- [13] R. Shnapp and V. Steinberg. Nonmodal elastic instability and elastic waves in weakly perturbed channel flow. *Phys. Rev. Fluids*, 7(6):063901, 2022.
- [14] V. Dzanic, C. S. From, and E. Sauret. The effect of periodicity in the elastic turbulence regime. *J. Fluid Mech.*, 937:A31, 2022.
- [15] D. W. Carlson, K. Toda-Peters, A. Q. Shen, and S. J. Haward. Volumetric evolution of elastic turbulence in porous media. *J. Fluid Mech.*, 950:A36, 2022.
- [16] S. Yamani, Y. Raj, T. A. Zaki, G. H. McKinley, and I. Bischofberger. Spatiotemporal signatures of elastoinertial turbulence in viscoelastic planar jets. *Phys. Rev. Fluids*, 8(6):064610, 2023.
- [17] G. Soligo and M. E. Rosti. Non-Newtonian turbulent jets at low-Reynolds number. *Int. J. Multiph. Flow*, 167:104546, 2023.
- [18] C. de Blois, S. J. Haward, and A. Q. Shen. Canopy elastic turbulence: Spontaneous formation of waves in beds of slender microposts. *Phys. Rev. Fluids*, 8(2):023301, February 2023.
- [19] S. R. Yerasi, J. R. Picardo, A. Gupta, and D. Vincenzi. Preserving large-scale features in simulations of elastic turbulence. *Journal of Fluid Mechanics*, 1000:A37, December 2024.

[20] E. Balkovsky, A. Fouxon, and V. Lebedev. Turbulence of polymer solutions. *Phys. Rev. E*, 64(5):056301, 2001.

[21] S. Berti, A. Bistagnino, G. Boffetta, A. Celani, and S. Musacchio. Two-dimensional elastic turbulence. *Phys. Rev. E*, 77(5):055306, May 2008.

[22] S. Berti and G. Boffetta. Elastic waves and transition to elastic turbulence in a two-dimensional viscoelastic Kolmogorov flow. *Phys. Rev. E*, 82(3):036314, September 2010.

[23] Z. Hong-Na, L. Feng-Chen, C. Yang, T. Kunugi, and Y. Bo. Direct numerical simulation of elastic turbulence and its mixing-enhancement effect in a straight channel flow. *Chinese Phys. B*, 22(2):024703, 2013.

[24] T. Watanabe and T. Gotoh. Power-law spectra formed by stretching polymers in decaying isotropic turbulence. *Phys. Fluids*, 26(3):035110, 2014.

[25] S. S. Ray and D. Vincenzi. Elastic turbulence in a shell model of polymer solution. *EPL*, 114(4):44001, 2016.

[26] D. Y. Li, H. Zhang, J. P. Cheng, X. B. Li, F. C. Li, S. Qian, and S. W. Joo. Numerical simulation of heat transfer enhancement by elastic turbulence in a curvy channel. *Microfluid. Nanofluid.*, 21(2):25, 2017.

[27] E. L. C. Plan, A. Gupta, D. Vincenzi, and J. D. Gibbon. Lyapunov dimension of elastic turbulence. *J. Fluid Mech.*, 822:R4, 2017.

[28] H. Garg, E. Calzavarini, G. Mompean, and S. Berti. Particle-laden two-dimensional elastic turbulence. *Eur. Phys. J. E*, 41(10):115, 2018.

[29] R. van Buel, C. Schaaf, and H. Stark. Elastic turbulence in two-dimensional Taylor-Couette flows. *EPL*, 124(1):14001, 2018.

[30] H. Garg, E. Calzavarini, and S. Berti. Statistical properties of two-dimensional elastic turbulence. *Phys. Rev. E*, 104(3):035103, 2021.

[31] M. Lellep, M. Linkmann, and A. Morozov. Purely elastic turbulence in pressure-driven channel flows. *PNAS*, 121(9):e2318851121, February 2024.

[32] R. K. Singh, P. Perlekar, D. Mitra, and M. E. Rosti. Intermittency in the not-so-smooth elastic turbulence. *Nat. Commun.*, 15(1):4070, 2024.

[33] P. Garg and M. E. Rosti. Elastic Turbulence Hides in the Small Scales of Inertial Polymeric Turbulence. *Phys. Rev. Lett.*, 135(7):074001, August 2025.

[34] G. I. Taylor. The Spectrum of Turbulence. *Proc. R. Soc. Lond. A*, 164(919):476–490, 1938.

[35] D. Mitra and R. Pandit. Dynamic multiscaling in fluid turbulence: An overview. *Phys. A: Stat. Mech. Appl.*, 318(1):179–186, February 2003.

[36] J. G. Oldroyd. On the formulation of rheological equations of state. *Proc. R. Soc. Lond. A*, 200(1063):523–541, 1950.

[37] R. B. Bird. *Dynamics of Polymeric Liquids, Volume 1: Fluid Mechanics*. Wiley, 1987.

[38] G. Foggi Rota, C. Amor, S. Le Clainche, and M. E. Rosti. Unified view of elastic and elastoinertial turbulence in channel flows at low and moderate Reynolds numbers. *Phys. Rev. Fluids*, 9(12):L122602, 2024.

[39] T. Dombre, U. Frisch, J. M. Greene, M. Hénon, A. Mehr, and A. M. Soward. Chaotic streamlines in the ABC flows. *J. Fluid Mech.*, 167:353–391, June 1986.

[40] V. Eswaran and S. B. Pope. An examination of forcing in direct numerical simulations of turbulence. *Comput. Fluids*, 16(3):257–278, January 1988.

[41] J. Jiménez and P. Moin. The minimal flow unit in near-wall turbulence. *J. Fluid Mech.*, 225:213–240, 1991.

[42] G. Buza, M. Beneitez, J. Page, and R. R. Kerswell. Finite-amplitude elastic waves in viscoelastic channel flow from large to zero Reynolds number. *J. Fluid Mech.*, 951:A3, November 2022.

[43] M. Beneitez, J. Page, and R. R. Kerswell. Polymer diffusive instability leading to elastic turbulence in plane Couette flow. *Phys. Rev. Fluids*, 8(10):L101901, October 2023.

[44] I Orlanski. A simple boundary condition for unbounded hyperbolic flows. *J. Comput. Phys.*, 21(3):251–269, July 1976.

[45] Y. Dubief, V. E. Terrapon, and B. Hof. Elasto-Inertial Turbulence. *Annu. Rev. Fluid Mech.*, 55(1):675–705, 2023.

[46] M. E. Rosti, P. Perlekar, and D. Mitra. Large is different: Nonmonotonic behavior of elastic range scaling in polymeric turbulence at large Reynolds and Deborah numbers. *Sci. Adv.*, 9(11):eadd3831, March 2023.

[47] M. S. Abdelgawad, I. Cannon, and M. E. Rosti. Scaling and intermittency in turbulent flows of elastoviscoplastic fluids. *Nat. Phys.*, pages 1–5, April 2023.

[48] J. Kim and P. Moin. Application of a fractional-step method to incompressible Navier-Stokes equations. *J. Comput. Phys.*, 59(2):308–323, 1985.

[49] R. Fattal and R. Kupferman. Time-dependent simulation of viscoelastic flows at high Weissenberg number using the log-conformation representation. *J. Nonnewton. Fluid. Mech.*, 126(1):23–37, February 2005.

[50] F. De Vita, M. E. Rosti, D. Izbassarov, L. Duffo, O. Tammisola, S. Hormozi, and L. Brandt. Elastoviscoplastic flows in porous media. *J. Nonnewton. Fluid. Mech.*, 258:10–21, August 2018.

[51] K. Sugiyama, S. Ii, S. Takeuchi, S. Takagi, and Y. Matsumoto. A full Eulerian finite difference approach for solving fluid–structure coupling problems. *J. Comput. Phys.*, 230(3):596–627, February 2011.

[52] M. Beneitez, J. Page, Y. Dubief, and R. R. Kerswell. Multistability of elasto-inertial two-dimensional channel flow. *J. Fluid Mech.*, 981:A30, February 2024.

[53] Yukio Kaneda, Takashi Ishihara, and Koji Gotoh. Taylor expansions in powers of time of lagrangian and eulerian two-point two-time velocity correlations in turbulence. *Physics of Fluids*, 11(8):2154–2166, 1999.

[54] VI Belinicher and VS L’vov. A scale-invariant theory of fully developed hydrodynamic turbulence. *Sov. Phys. JETP*, 66(2):303–313, 1987.

[55] Dhrubaditya Mitra and Rahul Pandit. Dynamics of passive-scalar turbulence. *Physical review letters*, 95(14):144501, 2005.

[56] M. Quadrio and P. Luchini. Integral time-space scales in turbulent wall flows. *Phys. Fluids*, 15(8):2219–2227, 2003.

[57] J. Kim, P. Moin, and R. Moser. Turbulence statistics in fully developed channel flow at low Reynolds number. *J. Fluid Mech.*, 177:133–166, 1987.

[58] Victor S L’vov, Evgenii Podivilov, and Itamar Procaccia. Temporal multiscaling in hydrodynamic turbulence. *Physical Review E*, 55(6):7030, 1997.

[59] Dhrubaditya Mitra and Rahul Pandit. Varieties of dynamic multiscaling in fluid turbulence. *Physical review letters*, 93(2):024501, 2004.

[60] Samriddhi Sankar Ray, Dhrubaditya Mitra, Prasad Perlekar, and Rahul Pandit. Dynamic multiscaling in two-dimensional fluid turbulence. *Physical Review Letters*, 107(18):184503, 2011.

[61] L. Biferale, E. Calzavarini, and F. Toschi. Multi-time multi-scale correlation functions in hydrodynamic turbulence. *Phys. Fluids*, 23(8):085107, 2011.

[62] Y. Kaneda, T. Ishihara, and K. Gotoh. Taylor expansions in powers of time of Lagrangian and Eulerian two-point two-time velocity correlations in turbulence. *Phys. Fluids*, 11(8):2154–2166, 1999.

[63] C. C. Lin. On Taylor’s Hypothesis and the Acceleration Terms in the Navier-Stokes Equations. *Q. Appl. Math.*, 10(4):295–306, 1953.

[64] J. L. Lumley. Interpretation of Time Spectra Measured in High-Intensity Shear Flows. *Phys. Fluids*, 8(6):1056–1062, 1965.

[65] U. Piomelli, J.-L. Balint, and J.M. Wallace. On the validity of Taylor’s hypothesis for wall-bounded flows. *Phys. Fluids A*, 1(3):609–611, 1989.

[66] A. Cenedese, G. P. Romano, and F. Di Felice. Experimental testing of Taylor’s hypothesis by L.D.A. in highly turbulent flow. *Exp. Fluids*, 11(6):351–358, 1991.

[67] S. Lee, S. K. Lele, and P. Moin. Simulation of spatially evolving turbulence and the applicability of Taylor's hypothesis in compressible flow. *Phys. Fluids*, 4(7):1521–1530, 1992.

[68] W. J. A. Dahm and K. B. Southerland. Experimental assessment of Taylor's hypothesis and its applicability to dissipation estimates in turbulent flows. *Phys. Fluids*, 9(7):2101–2107, 1997.

[69] A. Belmonte, B. Martin, and W. I. Goldburg. Experimental study of Taylor's hypothesis in a turbulent soap film. *Phys. Fluids*, 12(4):835–845, 2000.

[70] B. Ganapathisubramani, K. Lakshminarasimhan, and N. T. Clemens. Determination of complete velocity gradient tensor by using cinematographic stereoscopic PIV in a turbulent jet. *Exp. Fluids*, 42(6):923–939, 2007.

[71] P. Moin. Revisiting Taylor's hypothesis. *J. Fluid Mech.*, 640:1–4, December 2009.

[72] S. Davoust and L. Jacquin. Taylor's hypothesis convection velocities from mass conservation equation. *Phys. Fluids*, 23(5):051701, 2011.

[73] N. Hutchins and I. Marusic. Evidence of very long meandering features in the logarithmic region of turbulent boundary layers. *J. Fluid Mech.*, 579:1–28, 2007.

[74] D. J. C. Dennis and T. B. Nickels. On the limitations of Taylor's hypothesis in constructing long structures in a turbulent boundary layer. *J. Fluid Mech.*, 614:197–206, 2008.

[75] C. Geng, G. He, Y. Wang, C. Xu, A. Lozano-Durán, and J. M. Wallace. Taylor's hypothesis in turbulent channel flow considered using a transport equation analysis. *Phys. Fluids*, 27(2):025111, 2015.

[76] Y. Cheng, C. Sayde, Q. Li, J. Basara, J. Selker, E. Tanner, and P. Gentine. Failure of Taylor's hypothesis in the atmospheric surface layer and its correction for eddy-covariance measurements. *Geophys. Res. Lett.*, 44(9):4287–4295, 2017.

[77] S. Roy, J. D. Miller, and G. H. Gunaratne. Deviations from Taylor's frozen hypothesis and scaling laws in inhomogeneous jet flows. *Commun. Phys.*, 4(1):1–8, 2021.

[78] T. Burghelea, E. Segre, and V. Steinberg. Validity of the Taylor hypothesis in a random spatially smooth flow. *Phys. Fluids*, 17(10):103101, 2005.

[79] Sadhitro De, Dhrubaditya Mitra, and Rahul Pandit. Uncovering the multifractality of lagrangian pair dispersion in shock-dominated turbulence. *Physical Review Research*, 6(2):L022032, 2024.

[80] A. Fouxon and V. Lebedev. Spectra of turbulence in dilute polymer solutions. *Phys. Fluids*, 15(7):2060–2072, July 2003.

[81] A. Gupta and D. Vincenzi. Effect of polymer-stress diffusion in the numerical simulation of elastic turbulence. *J. Fluid Mech.*, 870:405–418, 2019.

[82] Stephen Childress. *Mechanics of swimming and flying*. Number 2. Cambridge University Press, 1981.